IEEE Access
Multidisciplinary ⋮ Rapid Review ⋮ Open Access Journal

Received May 9, 2021, accepted July 12, 2021, date of publication July 26, 2021, date of current version August 9, 2021.

Digital Object Identifier 10.1109/ACCESS.2021.3100546

Fast Diffusion Kurtosis Mapping of Human Brain at 7 Tesla With Hybrid Principal Component Analyses

FANGRONG ZONG[1], JIAXIN DU[2], XIAOFENG DENG[3,4], XUBIN CHAI[5], YAN ZHUO[5], A. VIKTOR VEGH[2], AND RONG XUE[5,6]

[1]Institute of Biophysics, China Academy of Sciences, Beijing 100101, China
[2]Centre for Advanced Imaging, The University of Queensland, St Lucia, QLD 4072, Australia
[3]Beijing Tiantan Hospital, Capital Medical University, Beijing 100070, China
[4]China National Clinical Research Center for Neurological Diseases, Beijing 100070, China
[5]State Key Laboratory of Brain and Cognitive Science, Institute of Biophysics, Chinese Academy of Sciences, Beijing 100101, China
[6]Sino-Danish College, University of Chinese Academy of Sciences, Beijing 100101, China

Corresponding author: Fangrong Zong (fangrong.zong@ibp.ac.cn)

This work was supported in part by the National Natural Science Foundation of China under Grant 61901465, and in part by the Chinese National Major Scientific Equipment Research and Development Project under Grant ZDYZ2010-2.

This work involved human subjects or animals in its research. Approval of all ethical and experimental procedures and protocols was granted by the Institutional Ethics Review Board.

ABSTRACT Diffusion kurtosis has become an important magnetic resonance imaging (MRI) modality for non-invasively mapping the microstructural variations in living tissues. Theoretically, the spatial resolution of diffusion kurtosis imaging (DKI) can be significantly improved by acquiring data at ultra-high magnetic fields (UHF, $\leq$ 7 Tesla) because of the increased signal-to-noise ratios. However, issues such as increased susceptibility artefacts and rapid signal attenuation inherent in UHF-MRI have impeded the adoption of DKI in research and clinics. In this paper, we developed a new image reconstruction algorithm for fast DKI at UHF. By integrating the one-dimensional and two-dimensional principal component analysis and compressed sensing technologies, the new algorithm can reconstruct kurtosis maps from highly undersampled data. The technique was validated using randomly undersampled brain images with a control database of fully sampled DKI acquisitions from healthy human participants. We compared the technique with zero-filling Fourier transform and similar compressed sensing algorithms by evaluating the peak signal-to-noise ratio (PSNR) and structural similarity index (SSIM) between images and assessing the reproducibility of results using the Bland-Altman method. We found that our methods can achieve at least a five-fold reduction in data acquisition time at UHF with high image quality. Moreover, the PSNR and SSIM of five diffusion metrics generated by our methods were superior to the other algorithms when the undersampling rate is high and the echo time is short. The proposed method can be valuable for fast functional and dynamic-contrast imaging techniques at 7 Tesla or higher.

INDEX TERMS Magnetic resonance imaging, ultra-high field, diffusion kurtosis imaging, principal component analysis, compressed sensing.

I. INTRODUCTION

Diffusion kurtosis metrics quantify the degree of deviation in water diffusion away from a Gaussian distribution. They have been shown to be more sensitive to tissue microstructure variations than the apparent diffusion coefficient (ADC) or diffusion tensor [1]–[4]. Measurements of kurtosis has become an important tool for assessing the progressive pathological changes between the brain in health and disease [5], [6]. It can be estimated from magnetic resonance imaging (MRI) data [2], [3], [7], [8] by using a high-order cumulant expansion mathematical model. The generation of kurtosis maps relies on diffusion-weighted imaging (DWI) data acquired using more than thirty diffusion directions and at least three diffusion weightings, or *b*-values [9] (i.e. diffusion kurtosis imaging, DKI). The signal-to-noise ratio (SNR) achieved by conventional DKI reconstruction is limited by the intrinsic magnetisation of tissue, i.e. produced by the magnetic field

The associate editor coordinating the review of this manuscript and approving it for publication was Gang Wang.

of the scanner, leading to low-resolution diffusion kurtosis maps in most research and clinic settings.

The development of ultra-high-field (UHF, $\geq$ 7 Tesla) MRI has significantly advanced diffusion-based imaging techniques, for example, to reveal sub-cortical structures in human brain by diffusion tensor imaging (DTI) [10]–[13]. While the high SNR achieved by UHF-MRI scanners offers great opportunities to improve the efficiency and image quality of DKI, the implementation of DKI at UHF has posed two key challenges. Firstly, the relatively short transverse relaxation time (T_2^*) of biological tissues at UHF causes increased signal attenuation at comparably long echo times (TE) that are usually required for DKI [14]. Secondly, large b-values (i.e. diffusion gradient amplitudes) that typically used at UHF induce significant eddy currents, which may result in image distortions. A substantial amount of research has been conducted to reduce the acquisition time of DKI, mostly by undersampling q-space, that is acquiring less number of diffusion directions [15]–[21].However, they neglect the importance of reducing echo time, a parameter mainly determined to encode the image with spatial information. On the other hand, undersampling in k-space could reduce the echo time [14], [22]. Higher k-space undersampling rate leads to smaller echo time. This approach automatically leads to a boost in SNR since less time is allowed for signal attenuation before data is collected. Moreover, less imaging time of UHF-DKI can provide an opportunity to average multiple datasets in one scan session, reducing accumulated image artefacts due to eddy currents and participant motion. One approach is to use parallel imaging [23] which has led to great improvements in DTI and DKI image quality at 3 T [24], [25]. However, the potentially significant increase in the specific absorption rate of radio frequency energy in tissue limits its application for 7 T DKI [26].

A reduction in echo time can be achieved by randomly undersampling k-space following a given trajectory [27]–[30]. Previous research has demonstrated that by exploiting a learning or combined sparse transforms in the compressed sensing (CS) framework [31]–[40], high resolution images from undersampled data can be reconstructed. Among these, one-dimensional principal component analysis (1D-PCA) have been utilised in obtaining T_1 and T_2 mappings from highly undersampled MRI data. It learns common features in the existing image databases to recover unsampled k-space during fast acquisition. In the meantime, the PCA reconstruction algorithms require less human interference and smaller databases as compared to the deep learning algorithms, which is of particular benefits for reconstructing data acquired at UHF as these datasets are not widely accessible. It offers great potential to apply PCA based methods in reconstructing the diffusion metrics from UHF DKI acquisition. The feasibility of applying the one-dimensional principal component analysis compressed sensing (1D-PCA-CS or PCA-CS) method to measure kurtosis using a 7 T MRI scanner is therefore investigated in this paper. To increase the reconstruction accuracy, we propose a novel hybrid-PCA reconstruction algorithm by incorporating two-dimensional PCA (2D-PCA) into the PCA-CS framework. The new algorithm is verified by varying sample rates in the participant data. Moreover, the existing DKI processing pipeline is optimised to retain the intrinsic signal-to-noise ratio (SNR) afforded by UHF and to correct for image distortions. The performance of the proposed algorithm is compared with the PCA-CS reconstruction method, and the zero-filling Fourier transform reconstruction, and evaluated by using peak SNR (PSNR) and structure similarity index (SSIM) values.

TABLE 1. The demographic data of the recruited participants.

	Male (n=10)	Female (n=12)	t	p
Age (years old)	19.75±1.29	20.25±1.55	0.861	0.398

II. MATERIALS AND METHODS

A. DATABASE CONSTRUCTION AND KURTOSIS ESTIMATION

This study included 22 healthy participants recruited from universities (10 male and 12 female) aged between 18-22 years. The demographic data of the healthy University students were listed in Table. 1. The experiment protocol was approved by the institutional ethics review board, and written informed consent was obtained from all participants prior to the scans. All MRI datasets were acquired using a 7 Tesla research scanner (Siemens Healthcare, Erlangen, Germany) equipped with a 1Tx/32Rx coil. Fully-sampled diffusion images were acquired using a spin-echo echo-planar imaging (SE-EPI) sequence with the following parameters: repetition time (TR)= 7 s, echo time (TE)= 55 ms, image matrix = 180 × 180 × 102, resolution = 1.5 mm × 1.5 mm ×1.5 mm, Field of View (FOV)= 27 cm × 27 cm × 15.3 cm, Number of excitation = 1, and multi-band factor = 2. DKI images were acquired with diffusion weighted factors of b = 1000 s/mm^2 in 30 directions and b = 2500 s/mm^2 in 60 directions. Two additional $b = 0$ s/mm^2 images were acquired with opposite phase encoding directions for motion correction (one with phase encoding from anterior to posterior, i.e., A-P direction, and the other one from posterior to anterior, i.e., P-A direction). The total acquisition time was 45 minutes for each participant.

Each dataset was checked qualitatively, and images with major issues (such as severe motion, signal drop out) were excluded from the analysis. The datasets were then corrected for artefacts caused by eddy currents, head motions, and field inhomogeneity [41]–[44]. This pre-processing yielded to 20 fully-sampled distortion-free datasets for the kurtosis reconstruction.

As the molecular diffusion in biological tissues is directional dependent, the kurtosis along a specific direction was obtained by fitting the fully-sampled datasets to the following equation using an iteratively weighted linear least square algorithm [45]:

$$S(b(n)) = S(0)\exp\left(-b(n)D(n) + \frac{b(n)^2 D(n)^2 K(n)}{6}\right), \quad (1)$$

where $b(n)$ represents the diffusion weighting factor when the gradient is applied along a specific direction, n. $S(b(n))$ is the measured DKI signal, and $D(n)$ and $K(n)$ are the diffusion and kurtosis values corresponding with direction n. To extend it into a three-dimensional model, $K(n)$ can be formulated from elements using a 4th-order tensor notation W_{ijkl} [1]. The 4th-order tensor has $m = 81$ elements, 15 of which are independent due to the symmetry of diffusion processes probed by DKI [7]. As a result, the estimation of the kurtosis tensor requires DWI data along at least 15 non-collinear and non-coplanar directions at each b value.

A higher value for $K(n)$ indicates that water molecule diffusion is further away from the Gaussian distribution than a low value for $K(n)$. The physical meanings of individual kurtosis elements are yet to be linked with specific biological properties of tissues due to the complexity of the 4th-order tensor. Nevertheless, the most practical kurtosis matrices that have been used in medical sciences are mean kurtosis (MK), axial kurtosis (AK) and radial kurtosis (RK). MK is the mean value of the overall kurtosis, which has no directional or dimensional information:

$$MK = \frac{1}{n}\sum_{i=1}^{n} K(n). \tag{2}$$

AK and RK are other dimensionless quantities but contain directional information which are defined as parallel and perpendicular to the principal diffusion tensor eigenvector (e_1) [46]:

$$AK = K_1, \tag{3}$$

$$RK = \frac{K_2 + K_3}{2}, \tag{4}$$

where $K_i (i = 1, 2, 3)$ are the kurtosis components, $K(n)$, projected to three eigenvectors of the diffusion tensor [47].

Besides kurtosis values, the fractional anisotropy (FA) and kurtosis FA (KFA) are dimensionless metrics that quantify the degree of diffusion anisotropy in tissues, which can be obtained through the DTI and DKI process shown in Eq. 5 and Eq. 6, respectively:

$$FA = \sqrt{\frac{1}{2}}\frac{\sqrt{(\lambda_1 - \lambda_2)^2 + (\lambda_1 - \lambda_3)^2 + (\lambda_2 - \lambda_3)^2}}{\sqrt{\lambda_1^2 + \lambda_2^2 + \lambda_3^2}}, \tag{5}$$

where $\lambda_i (i = 1, 2, 3)$ are the orthogonal diffusion components ($D(n)$) projected to three eigenvectors of the diffusion tensor.

$$KFA = \frac{||\mathbf{W} - \mathrm{WI}||}{||\mathbf{W}||}, \tag{6}$$

where $\mathbf{W}$, W and $\mathbf{I}$ are the normalized value of the kurtosis tensor, the mean value of $\mathbf{W}$ and the 4th rank of the isotropic tensor, respectively. As with FA, the normalization gives that the KFA values range from 0 (isotropic) to 1 (extreme anisotropic).

Our data analysis mainly utilises the functions provided in Functional Magnetic Resonance Imaging of the Brain Software Library (FSL) 5.09 (https://www.fmrib.ox.ac.uk/fsl), Advanced Normalization Tools (ANTs) (https://www.nitrc.org/projects/ants) and Diffusion Kurtosis Estimator (DKE) (https://www.nitrc.org/projects/dke). The processing pipelines and final outputs are summarised in Fig. 1.

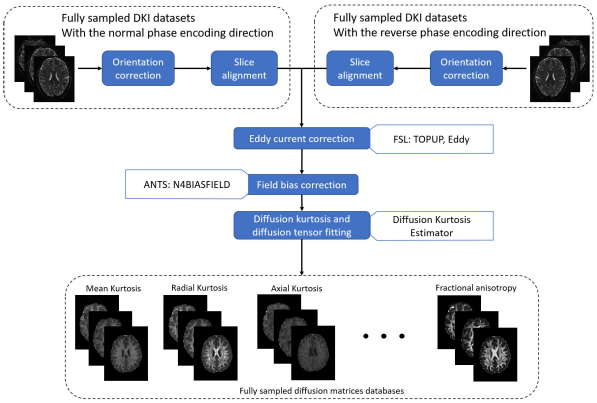

FIGURE 1. The DKI data processing pipeline used in this work. Fully sampled DKI datasets with the normal and reverse phase encoding directions were obtained according to the acquisition parameters (described in section II. A.) firstly, followed by orientation correction and slice alignments. The datasets were then corrected for effects caused by eddy currents, head motions, and field inhomogeneity by the topup and eddy functions in *fsl* and the N4biasfield function in *Ants*. After using the diffusion kurtosis estimator software, multiple parameters were extracted to build the fully sampled diffusion matrices databases.

B. UNDERSAMPLING PATTERNS

After the full k-space data was acquired from the 7 T MRI scanner using the aforementioned SE-EPI sequence, a random in-plane undersampling pattern were designed for one participant under study to obtain the incomplete k-space data following the strategy described in Ref. [36]. Here we chose the undersampling along the phase encoding direction, which inherently reduces distortions related to echo planer imaging (EPI) readouts. For simplicity, the same in-plane undersampling patterns were applied to each slice and volumetric undersampled DKI datasets were generated. Fig. 2 (a) shows a mask with 20% sampling along phase-encoding direction, and Fig. 2 (b) and (c) shows the zero-filling Fourier Transformed (FT) images of two k-space datasets acquired using the mask and two different b-values. Compared to the fully-sampled image (Fig. 2 (d)), the undersampled images exhibit less distortion but more aliasing artefacts. These artefacts can be removed using iterative thresholding algorithms since they are incoherent with the raw signal [48]–[50]. The kurtosis maps of the undersampled datasets were generated using the same DKE pipeline as for the fully-sampled datasets, and are referred to as *undersampled kurtosis maps*. It shall be noted that the undersampled DWI images were not processed by using either FSL or ANT's functions which were only operated on the fully sampled images.

C. THE PCA RECONSTRUCTION ALGORITHMS

Both 1D-PCA [51] and 2D-PCA [52] are widely used to analyse datasets containing elements that are described by multiple intercorrelated variables. The objective of PCA algorithms is to extract the main features (i.e. principal

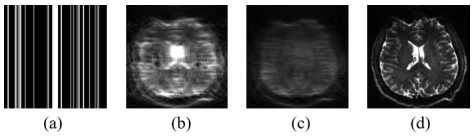

FIGURE 2. Under-sampling results with 5-fold acceleration: (a) undersampling pattern [36]; (b) zero-filling FT b_0 image; (c) zero-filling FT b_{1000} image; (d) fully sampled b_0 image. In (a), The white stripes indicate that the corresponding *k*-space area was retained, and the black stripes indicate the zero-filled *k*-space areas.

components) from the database and express the information using a set of new uncorrelated variables (aka over an orthogonal bases), so that each element in the database can be reconstructed using a combination of the orthogonal bases with corresponding weighting factors. Such a multi-variate technique has previously been used in pattern recognition, and later extended to image compression and MRI image reconstruction [34], [51]–[56]. In these applications, 1D-PCA is usually combined with compressed sensing to reconstruct either temporally- or spatially-undersampled MRI data, commonly referred to as PCA-CS [38], [57], [58], but the reconstructed errors are larger than a machine learning algorithm using 2D-PCA. To increase the reconstruction accuracy based on PCA-CS, we propose a novel hybrid-PCA reconstruction algorithm by incorporating the 2D-PCA into the PCA-CS algorithm. The flowchart of 1D- and 2D-PCA are given in details before the new hybrid-PCA reconstruction algorithm.

1) THE 1D-PCA ALGORITHM

The procedure of obtaining the principal component basis via 1D-PCA is illustrated by Fig. 3. The database can be images or features that are generated by other algorithms (such as 2D-PCA in our case). Each of the d images in the database $(\mathbf{I}_1, \mathbf{I}_2, \ldots, \mathbf{I}_d)$ is firstly re-arranged into a vector $(\vec{I}_1, \vec{I}_2, \ldots, \vec{I}_d)$, thus the database can be treated as a $L \times d$ matrix ($\mathbf{D}_\mathrm{B}$). Subsequently, a covariance matrix $\mathbf{C}$ is constructed from the database matrices:

$$\mathbf{C} = (\mathbf{D}_\mathrm{B} - \mathbf{M}_\mathrm{B})^T (\mathbf{D}_\mathrm{B} - \mathbf{M}_\mathrm{B}). \tag{7}$$

$\mathbf{M}_\mathrm{B}$ is a $L \times d$ matrix whose columns are identical and equal to the vectorised mean image:

$$\vec{I}_\mathrm{m} = \frac{1}{d} \sum_{n=1}^{d} \vec{I}_n. \tag{8}$$

The elements in the covariance matrix represent the correlation of each pixel among the images in the database. The eigenvectors of 1D-PCA ($\mathbf{U}_\mathrm{1D}$) can be determined by diagonalising the covariance matrix $\mathbf{C}$, and they are ordered according to their corresponding eigenvalues. Projecting the matrix $(\mathbf{D}_\mathrm{B} - \mathbf{M}_\mathrm{B})$ on $\mathbf{U}_\mathrm{1D}$ yields the principal component matrix of the database

$$\mathbf{PC}_\mathrm{1D} = (\mathbf{D}_\mathrm{B} - \mathbf{M}_\mathrm{B}) \cdot \mathbf{U}_\mathrm{1D}. \tag{9}$$

The size of $\mathbf{PC}$ is also $L \times d$, in which the column vectors are referred to as the principal components [53], and they are orthonormal to each other. Individual images in the database

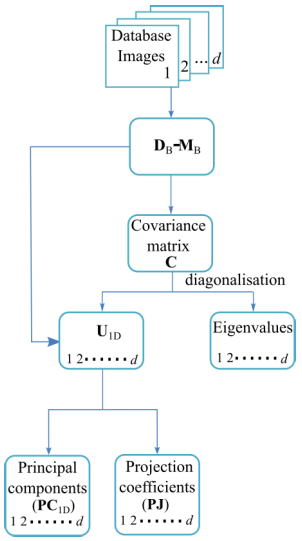

FIGURE 3. Flow chart of the 1D-PCA procedure. $\mathbf{M_B}$ is a $L \times d$ matrix in which the columns are identical, equal to the vectorised mean image; $\mathbf{U_{1D}}$ is a $d \times d$ matrix containing the eigenvectors after eigen-decomposing the covariance matrix C. PJ are the full set of coefficients.

can be reconstructed using the principal components together with suitable weighting factors that are used to characterise this image (i.e., projection coefficients **PJ** in Fig. 3). These weighting factors can be determined by projecting this image to the principal component basis.

Because most elements in **PJ** carries negligible weighs (approximate zero), the corresponding principal components can therefore be used as a sparse domain. The sparsity of this orthonormal basis is measured by the ratio of the number of zero-elements to the number of total elements.

2) THE 2D-PCA ALGORITHM

The 2D-PCA algorithm was proposed by Yang *et al.* [52] for feature extraction and data representation, and has been applied to reconstruct highly undersampled MRI data [36]. It directly processes the 2D matrices to extract independent features from the image. The image covariance matrix ($\mathbf{C}$) of 2D-PCA is constructed by using the original d images which are represented by $M \times N$ matrices:

$$\mathbf{C} = \frac{1}{d} \sum_{i=1}^{d} (\mathbf{I}_i - \hat{\mathbf{I}})^T (\mathbf{I}_i - \hat{\mathbf{I}}), \tag{10}$$

where $\mathbf{I}_i$ is the i-th image and $\hat{\mathbf{I}}$ is the mean image matrix. The size of the covariance matrix $\mathbf{C}$ is N by N where N is the size of the column of the image. Each element in $\mathbf{C}$ is the average of the correlation coefficients between columns in this set of images. By diagonalising $\mathbf{C}$, a matrix of eigenvectors of 2D-PCA ($\mathbf{U}_\mathrm{2D}$) along with their corresponding eigenvalues are obtained:

$$\mathbf{U}_\mathrm{2D}^T \cdot \mathbf{C} \cdot \mathbf{U}_\mathrm{2D} = \begin{bmatrix} \lambda_1 & 0 & \cdots & 0 \\ 0 & \lambda_2 & \cdots & 0 \\ \vdots & \vdots & \ddots & \vdots \\ 0 & 0 & \cdots & \lambda_d \end{bmatrix}, \tag{11}$$

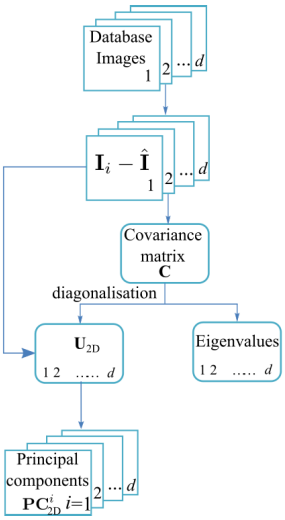

FIGURE 4. Flow chart of the 2D-PCA procedure. $\mathbf{I}_i$ and $\hat{\mathbf{I}}$ are the *i*-th and the mean image matrices, respectively. $\mathbf{PC}^1_{2D}, \ldots, \mathbf{PC}^d_{2D}$ are the principal components of the database.

where $(\lambda_{1,2,3})$ are the eigenvalues. These eigenvectors in $\mathbf{U}_{2D}$ have been proven to be the optimal axis for feature extraction [52]. The feature matrix $(\mathbf{PC}^i_{2D})$ of the i^{th} image can be obtained by projecting the 2D image matrix on $\mathbf{U}_{2D}$ directly:

$$\mathbf{PC}^i_{2D} = (\mathbf{I}_i - \mathbf{I}) \cdot \mathbf{U}_{2D}, \tag{12}$$

where $\mathbf{PC}^i_{2D}$ is a $M \times N$ matrix, whose columns are the principal components of the image. After projecting all the images in the database to $\mathbf{U}_{2D}$, a 3D dataset of principal component matrices $(\mathbf{PC}^1_{2D}, \ldots, \mathbf{PC}^d_{2D})$ is built for further analysis. The procedure of 2D-PCA is illustrated in Fig. 4. It is worth noting that the 2D-PCA algorithm cannot be directly integrated in to the CS scheme as the feature space is not sparse. However, it is possible to modify the original PCA-CS algorithm via integrating the 2D-PCA to improve the reconstruction accuracy.

3) THE HYBRID-PCA RECONSTRUCTION ALGORITHM

The new hybrid-PCA reconstruction algorithm illustrated in Fig. 5 approximates the undersampled image by iteratively improving estimations for the missing *k*-space data. The database images $(1, 2, \ldots, d)$ in Fig. 5 are from the fully sampled kurtosis datasets $(d = 20)$. By applying the 2D-PCA toolbox on the database, an eigenvector set of $\mathbf{U}_{2D}$ and eigenvalues are generated through Eq. (11). In the next step, through the projection of the de-centralised b_0 maps of individual participants, we build a 3D principal components matrix with elements being 2D principal components $\mathbf{PC}^i_{2D}$ for each participant. The 3D feature matrix is further processed by 1D-PCA forming a 2D principal components matrix ($\mathbf{PC}_{1D}$) which has lower rank and higher sparsity, i.e. $\mathbf{D}_B$ in Fig. 3 is constructed by $\mathbf{PC}^i_{2D}$ $(i = 1, 2, \ldots, d)$. Meanwhile, the undersampled kurtosis maps are projected to $\mathbf{U}_{2D}$ to generate the undersampled principal component PC'_{2D}. After the sparse feature domain and undersampled principal components PC'_{2D} have been generated, signal recovery is achieved through an iterative l_1 norm optimisation approach:

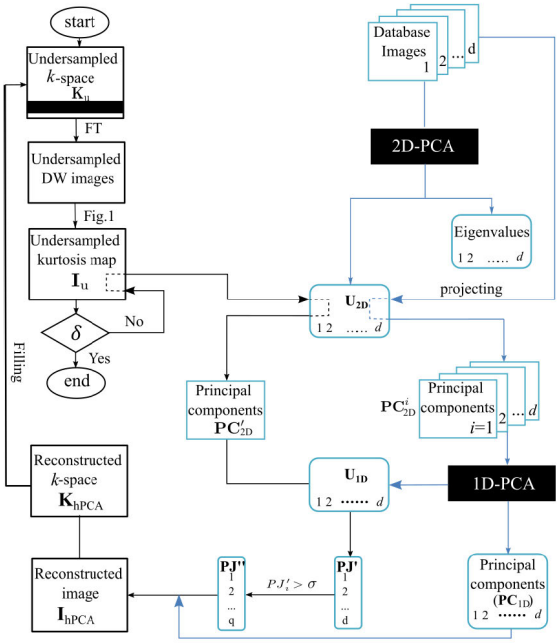

FIGURE 5. The framework of the hybrid-PCA reconstruction algorithm. The black boxes are the procedures of 1D-PCA and 2D-PCA algorithms. The reconstruction procedure started with randomly undersampling *k*-space (the black lines symbolise the un-sampled areas), and iterated until Eq. (13) is satisfied. The database images were converted to a feature base by utilising 2D-PCA, followed by a common CS MRI procedure which sparse transformation domain is consisted of the principal components obtained by 1D-PCA. While $\mathbf{PJ}'$ were the full set of coefficients of projecting the undersampled image to the principal components, $\mathbf{PJ}''$ represents the truncated set due to the l_1 and l_2 minimisation as is given by Eq. (13).

$$\text{argmin } ||\Phi\hat{x}||_1, \quad \text{subject to } ||\Psi\hat{x} - y||_2 < \delta, \tag{13}$$

where $\hat{x}$ and y are the estimated (reconstructed) signals and measurements, respectively. Ψ is the transform from the signal to measurements, and Φ is the sparse transform of the signal which is $\mathbf{PC}_{1D}$ in our case. δ is the threshold to control data consistency. $||\cdot||_1$ and $||\cdot||_2$ are the l_1 norm (sum of the absolute elements) and the l_2 norm (sum of squared elements and then square root), respectively. In specific, a subset of $\mathbf{PJ}'$ will be chosen to form a new vector $\mathbf{PJ}''$ if $\mathbf{PJ}' > \sigma$. Afterwards, an image $\mathbf{I}_{hPCA}$ can be reconstructed by this truncated $\mathbf{PJ}''$ vector and its corresponding principal components $\mathbf{PC}_{1D}$. The *k*-space data $\mathbf{K}_{hPCA}$ is then obtained through the inverse FT of $\mathbf{I}_{PCA}$ and used to update the undersampled *k*-space data, $\mathbf{K}_u$. An updated undersampled image $\mathbf{I}_u$ is then obtained by applying the FT operator of the updated *k*-space and used as the input for the next iteration. The reconstruction procedure of this undersampled image will be iterated until the Euclidean distance of the neighbouring two output $\mathbf{I}_u$ is smaller than δ.

D. PERFORMANCE EVALUATIONS

The performances of different algorithms were evaluated quantitatively using PSNR and SSIM which were calculated

on the whole brain regions after skull striping. PSNR measures the intensity differences between the reconstructed and original kurtosis images, and is defined by [59]:

$$\mathrm{PSNR} = 20\log_{10}\left(\frac{\mathrm{MAX}}{\sqrt{\mathrm{MSE}}}\right), \tag{14}$$

where MSE is the mean squared error of the image and MAX is the maximum pixel imaging intensity of the image. Served as a performance criterion, all levels of PSNR will be acceptable in this work. SSIM [60] estimates the differences of two images in terms of luminance, contrast, as well as structural changes in a user-defined window, defined as:

$$\mathrm{SSIM}(\mathbf{a},\mathbf{b}) = \frac{2\mu_{\mathbf{a}}\mu_{\mathbf{b}} + \mathrm{c}_1}{\mu_{\mathbf{a}}^2 + \mu_{\mathbf{b}}^2 + \mathrm{c}_1} \cdot \frac{2\sigma_{\mathbf{a}}\sigma_{\mathbf{b}} + \mathrm{c}_2}{\sigma_{\mathbf{a}}^2 + \sigma_{\mathbf{b}}^2 + \mathrm{c}_2} \cdot \frac{\sigma_{\mathbf{ab}} + \mathrm{c}_3}{\sigma_{\mathbf{a}} + \sigma_{\mathbf{b}} + \mathrm{c}_3}, \tag{15}$$

where $\mu_{\mathbf{a}}$ and $\mu_{\mathbf{b}}$ represent the mean value of the original and reconstructed images $\mathbf{a}$ and $\mathbf{b}$, respectively. $\sigma_{\mathbf{a}}$ and $\sigma_{\mathbf{b}}$ are the standard deviations, and $\sigma_{\mathbf{ab}}$ is the covariance of the two images. Constants c_1, c_2 and c_3 are introduced to avoid numerical error as denominators approach zero. By definition, SSIM is in the range -1 to 1, and equals to 1 only when $\mathbf{a} = \mathbf{b}$. SSIM is calculated for a set of 11×11 windows, which are displaced voxel-by-voxel until the entire image is visited. The mean SSIM is used as a similarity measure between the original and reconstructed images.

III. RESULTS AND DISCUSSION

A. DISTORTION CORRECTION

The b_0 images before and after the distortion correction are provided in Fig. 6. The artefacts in EPI images cause by imaging field inhomogeneity is significantly higher at UHF [60]. As shown in Fig. 6(b), the frontal lobe is stretched in the image, the phase encoding direction of which is the inverse of Fig. 6(a). By maximising the similarity of paired b_0 images acquired with opposite phase-encoding directions, we estimated the phase difference between them, which can be used to correct for these distortions [61]. As shown in Fig. 6, the image intensity is much higher in the occipital lobe than in the frontal lobe. This are likely caused by the bias field effects that are introduced by the dielectric resonance artefact and electromagnetic field non- uniformity, the severity of which amplifies at UHF. These effects are apparent in both Fig. 6(a) and (b), suggesting they are independent of the phase encoding direction. The least squares B-Spline algorithm proposed by Tustison et. al [62] were used to correct for these distortions.

As depicted in Fig. 6(c), the post-processing procedures removed most of the artefacts caused by eddy currents and bias fields, enabling one to generate distortion-free diffusion images from which kurtosis maps are derived. Fig. 7 elucidates an example of the MK images at 7 T before and after the corrections. For comparison, the same participant underwent an additional DKI scan at 3 T (Siemens Healthcare, Erlangen, Germany) with the same protocol/acquisition parameters as 7 T (introduced before) except that the in-plan resolution was

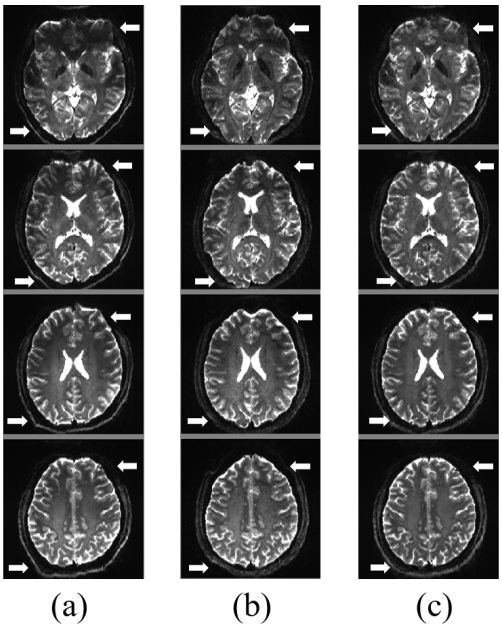

FIGURE 6. The b_0 images of different slices from a healthy volunteer before and after distortions. (a) acquired at 7 Tesla scanner with A-P phase encoding direction; (b) acquired at 7 Tesla scanner with P-A phase encoding direction and (c) after distortion correction.

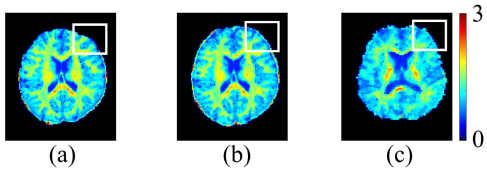

FIGURE 7. The mean kurtosis (MK) images (a) without distortion correction at 7 T; (b) with distortion correction at 7 T; (c) with distortion correction at 3 T.

set to 2 mm. The result are shown in Fig. 7(c). It is evident that the 7 T kurtosis map contained a higher level of detail about the brain structure than the 3 T reconstruction, an observation consistent with previous findings [63]. In particular, the grey-white matter boundaries inside the highlighted region were more conspicuous at 7 T than at 3 T, refer to Fig. 7.

The corrected MK map at 7 T suppresses the distortions in the highlighted region in Fig. 7 and revealed finer structures than observable at 3 T. These results suggest that DKI performs better at UHF provided appropriate post-processing is applied to the data. Furthermore, the kurtosis maps of the same brain produced at 3 T and 7 T were visually different after skull stripping, which indicates that a standardisation procedure needs to be established for the DKI acquisition and processing across different field strengths. A resolution of 1.5 mm isotropic fully-sampled DKI maps were obtained in this study. It is mainly because that the magnetic field of 7 T brings high signal to noise ratio along with the 45-minute scanning. Such long acquisition time may not be feasible for clinic use. Our fast acquisition technique and image reconstruction algorithms enabled one to retain the 1.5 mm isotropic resolution for DKI with significant reduced acquisition time.

TABLE 2. Comparison of the PSNR and mean SSIM of MK maps with different reconstruction methods in one subject (undersampling rate = 80%).

Measures	zero-filling FT	PCA-CS	hybrid-PCA
PSNR	15.83±3.16	18.91±3.78	24.78±4.85
SSIM	0.73±0.10	0.76±0.11	0.88±0.15

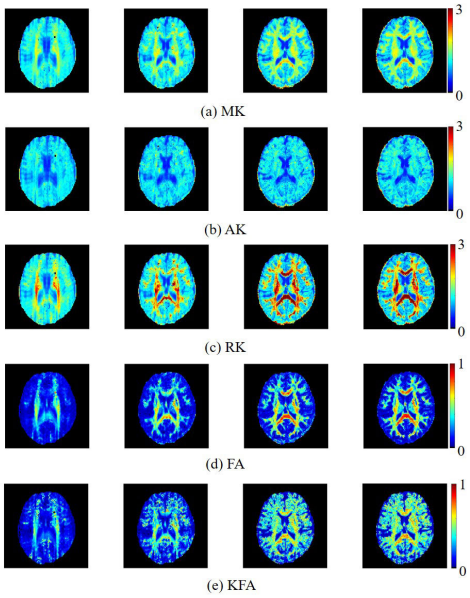

FIGURE 8. The reconstructed maps of different diffusion metrics ((a) MK, (b) AK, (c) RK, (d) FA, (e) KFA) from the corresponding under-sampling cases in Fig.2. The images from left to right are the results from the zero-filling, PCA-CS reconstruction, hybrid-PCA reconstructions and fully sampled diffusion matrices' maps, respectively.

B. HYBRID-PCA RECONSTRUCTION AND REPRODUCIBILITY

To evaluate the performance of the proposed method, one subject was randomly selected of which the fully-sampled *k*-space were undersampled according to the description in section II. B. The hybrid-PCA reconstruction algorithm was then used to recover the upsampled *k*-space, and compared with the zero-filling Fourier Transform (FT) and PCA-CS algorithms. Table. 2 summaries the PSNR and mean SSIM values of the MK maps reconstructed using three algorithms across 30 different slices away from the isocenter. The hybrid-PCA algorithm performed the best among the three algorithms with the PSNR being about 31% higher than that of the PCA-CS, which itself is about 20% higher than that of the zero-filling FT. The mean SSIM of hybrid-PCA was 0.88, thereby outperforming PCA-CS and zero-filling FT by 15% and 20%, respectively. These quantitative measures demonstrate the achievable performance of the hybrid-PCA algorithm in the reconstruction of UHF kurtosis maps.

The new hybrid-PCA algorithm was also used to reconstruct other diffusion metrics besides MK. In the same vein, maps for AK, RK, FA and KFA were generated from the same datasets (see Fig. 8 for results and Fig. 9 for reconstruction errors). The hybrid-PCA reconstruction algorithm produced visually clearer grey-white matter boundaries across

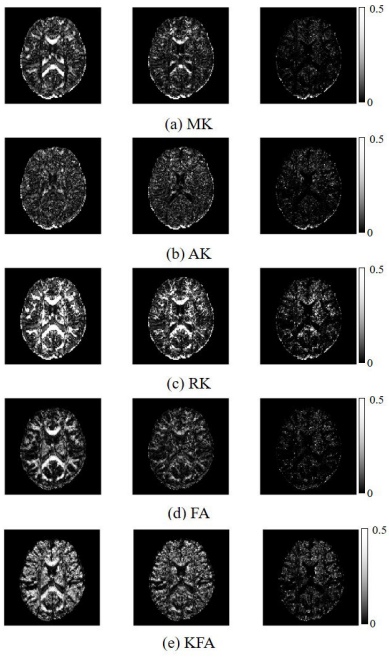

FIGURE 9. The reconstructed error images of different algorithms with four diffusion metrics ((a) MK, (b) AK, (c) RK, (d) FA, (e) KFA) from the corresponding slices in Fig. 8. The images from left to right are the results from the zero-filling, PCA-CS, hybrid-PCA reconstruction and fully sampled maps, respectively.

all diffusion metrics reported. The best grey-white matter contrast was observed in the FA images, followed by the RK, KFA, MK and AK images. Whereas, the best sub-cortical grey-white matter and cerebrospinal fluid contrasts appear to present in the KFA maps, followed by the AK, MK, RK and FA results. This suggests that KFA and AK may be more sensitive to tissue differences in comparison with FA, and could potentially be used as a biomarker for diseases and disorders affecting the cerebral cortex. This is in line with previous finding that KFA has been demonstrated to provide supplementary contrast to FA [64].

It is worth mentioning that one crucial element to reconstruct the undersampled kurtosis maps is the undistorted database as the input of the hybrid-PCA algorithms in our study. As a result, the proposed hybrid-PCA algorithm may have no advantages in reconstructing the kurtosis maps if the database is of low quality (for instance acquired from different scanners or from different age groups). Moreover, this database excludes participants with mental diseases, and therefore, is not suitable to be used for reconstructing diseased brains. However, its performance may be improved if the database is expanding, thus increasing the probability of having more similar features in the database. If the database is constructed of distorted images, one may be able to perform more advanced distortion correction algorithms after the hybrid-PCA reconstruction which is beyond the scope of the current study.

To investigate the reproducibility of the hybrid-PCA results, we randomly selected additional 10 datasets to perform image reconstruction at the undersampling rate of 80%. The variations of PSNR and mean SSIM differences between

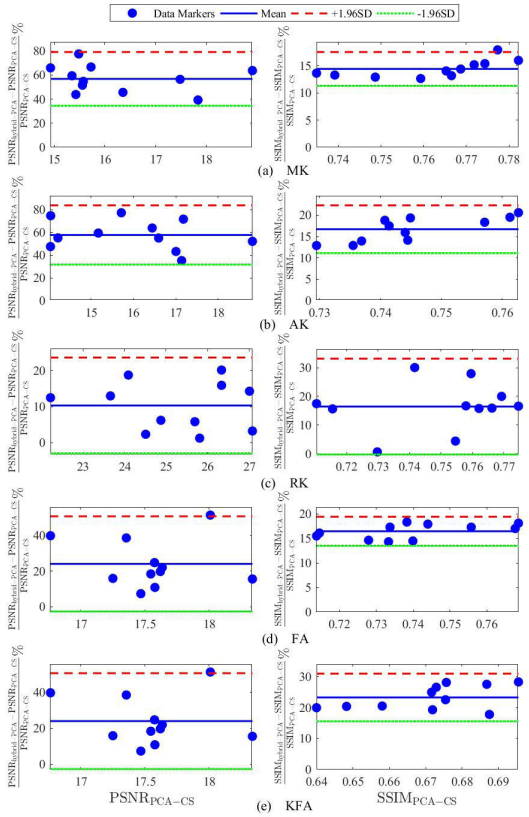

FIGURE 10. The bland-altman plots of PSNR (left) and mean SSIM (right) of four diffusion metrics ((a) MK, (b) AK, (c) RK, (d) FA, (e) KFA) maps reconstructed from the PCA-CS and hybrid-PCA algorithms at the sampling rate of 0.2.

PCA-CS and hybrid-PCA reconstruction algorithms across participants are shown in Fig. 10. The horizontal (i.e. x-) axes are the PSNR (left) and mean SSIM (right) values of the PCA-CS method, and the vertical axes are the difference between two methods. The blue solid line represents the mean differences between PCA-CS and hybrid-PCA reconstruction algorithms. The red dash line and green dotted line indicate upper and lower limits of agreement at 95% confidence interval between PCA-CS and hybrid-PCA reconstruction algorithms. It can be found from Fig. 10 that 95% of the data points lie within the limits of agreements for all four diffusion metrics, demonstrating that the hybrid-PCA method performs better than PCA-CS in all participants studied. For example, at the 80% undersampling rate, the PSNR of hybrid-PCA in reconstructing the MK map is consistently 50% higher than the PSNR of PCA-CS across all participants. The largest differences between two methods were observed in reconstructing AK maps whereas the smallest differences were shown in the reconstruction of RK maps.

C. HYBRID-PCA PERFORMANCE WITH DIFFERENT SAMPLING RATES

We further tested the hybrid-PCA reconstruction algorithms at various sampling rates. The mean PSNR and SSIM values of MK maps at 10 different sampling rates (0.1, 0.2, 0.3, 0.4, 0.5, 0.6, 0.7, 0.8, 0.9, 0.95) are reported in Fig. 11.

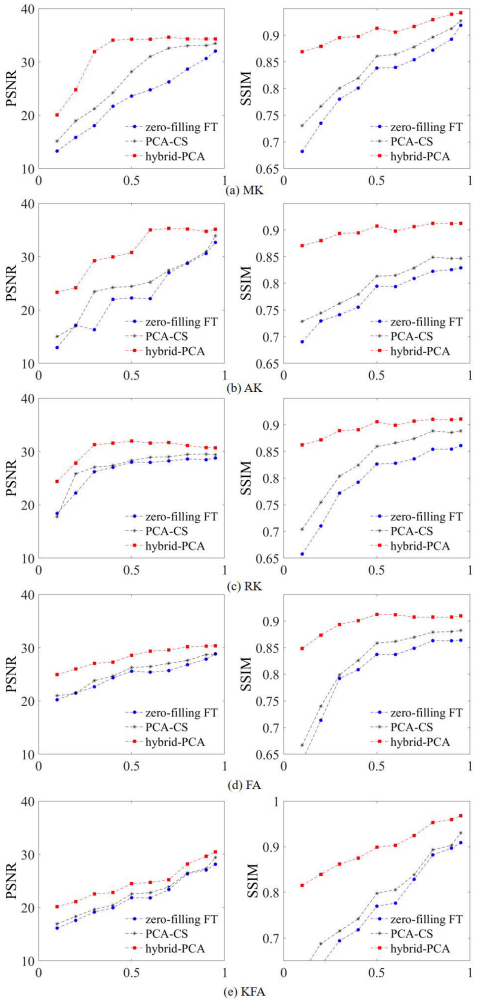

FIGURE 11. The mean PSNR and SSIM values of four diffusion metrics ((a) MK, (b) AK, (c) RK, (d) FA, (e) KFA) maps reconstructed from the zero-filling FT, PCA-CS and hybrid-PCA algorithms at sampling rates of 0.1, 0.2, 0.3, 0.4, 0.5, 0.6, 0.7, 0.8, 0.9 and 0.95, respectively.

As expected, the PSNR of the hybrid-PCA increased with a decrease in undersampling. At all tested sampling rates, the hybrid-PCA algorithm produced a consistently higher PSNR than the PCA-CS or zero-filling FT algorithms. At the 90% undersampling rate, the PSNR of the hybrid-PCA was about 32% and 51% higher than PCA-CS and zero-filling FT, respectively. With an decrease in the undersampling rate, the PSNR of the hybrid-PCA improved much faster than the other two methods, and it also saturated at a much lower sampling rate (around 60% undersampling). The PSNR of PCA-CS saturated at the 70% undersampling rate, and the zero-filling FT was not saturated. The PSNR differences were much smaller at the 10% undersampling rate with the hybrid-PCA outperforming the PCA-CS and zero-filling FT by only 4% and 12%. At all sampling rates, the mean SSIM of hybrid-PCA remained above 0.85, which was consistently higher than the mean SSIM of PCA-CS or zero-filling FT. The difference was more pronounced at high undersampling rates ($\leq 50\%$). At the undersampling rates of 90%, 50% and 10%, the mean SSIM value of hybrid-PCA was about 14%,

5% and 3% higher than PCA-CS, which was about 28%, 9% and 5% higher than zero-filling FT, respectively. At zero undersampling (i.e. fully sampling), the PSNR and SSIM values of the hybrid-PCA algorithm are expected to be the same as the zero-filling FT. This is because that the sampled *k*-space is retained in the hybrid-PCA algorithm whilst only the unsampled *k*-space is filled iteratively.

We observed similar trends in the other reconstructed diffusion metrics, refer to Fig. 11 (c). For the FA and KFA maps (Fig. 11 (d) and (e)), the PSNR decreased almost linearly with undersampling rates, which was ascribed to the high tissue contrast-to-noise ratio achieved in the FA map construction. However, the contrast-to-noise ratio was found to be much lower in the AK maps, leading to substantial fluctuations in the PSNR (Fig. 11 (b)).

IV. CONCLUSION

This work firstly investigated the feasibility of obtaining high-quality diffusion kurtosis maps from highly undersampled *k*-space data with the PCA-CS techniques. The kurtosis data were measured at an UHF MRI system with the static field strength of 7 T. As large-scale kurtosis databases are not widely available at 7 T, reconstruction of these maps by using existing deep learning methods are limited. We therefore proposed a hybrid-PCA reconstruction algorithm to recover the mean, axial and radial kurtosis parameters, in addition to producing diffusion fractional anisotropy and kurtosis fractional anisotropy maps with higher accuracy than conventional PCA-CS algorithms. It relates to a 5-fold improvement in data acquisition times for UHF DKI. Essentially, the proposed hybrid-PCA technique for kurtosis mapping integrates 1D-PCA and 2D-PCA into a CS framework, resulting in improved PSNR and mean SSIM values than those for the PCA-CS algorithm based on a group of randomly selected participants.

The hybrid-PCA reconstruction algorithm was additionally evaluated in terms of *k*-space undersampling rates. We found that the hybrid-PCA reconstruction provided superior mean kurtosis and fractional anisotropies maps with as much as 90% undersampled *k*-space data. Among the five representative diffusion metrics considered, our results suggest that kurtosis fractional anisotropy, radial kurtosis and fractional anisotropy provided higher tissue contrast than axial kurtosis evaluated by PSNR and SSIM values. Other diffusion metrics obtainable by the DKI processing framework requires further exploration and evaluation.

Several limitations must be considered in the present study. First, the databases were acquired on a single MR scanner and from healthy participants with a narrow range of age, restricting the undersampled images with similar/same conditions. Second, while the resolution of 1.5 mm isotropic for kurtosis maps were achieved in this study, it is mainly due to high magnetic field scanner used in the study. The hybrid-PCA algorithm allows for less imaging time and less distortions as induced by the high field. Third, we performed the artifact corrections on the fully sampled datasets instead of the undersampled images. Future studies may need to address the feasibility of applying eddy and motion corrections on undersampling k-space datasets. Fourth, only PSNR, SSIM and error images were used for evaluating the performance of the hybrid-PCA algorithms, other measures such as line profiles can be applied to investigate local variations and performance of the algorithm. Nevertheless, the protocol is reasonable for demonstrating the feasibility of the proposed hybrid-PCA algorithm on UHF DKI data.

In conclusion, our hybrid-PCA reconstruction algorithm is a reliable approach for reconstructing distortion-free, multi-parametric diffusion kurtosis and fractional anisotropy maps from UHF DKI data. The method is able to recover more diffusion information from undersampled data than existing principal component analysis compressed sensing methods, especially when reduced scan times are to be achieved via high *k*-space undersampling rates. The proposed approach can potentially be extended to reconstructing parametric maps for other MRI modalities that share similarities with the diffusion kurtosis imaging data collection process.

REFERENCES

[1] J. H. Jensen, J. A. Helpern, A. Ramani, H. Lu, and K. Kaczynski, "Diffusional kurtosis imaging: The quantification of non-Gaussian water diffusion by means of magnetic resonance imaging," *Magn. Reson. Med.*, vol. 53, no. 6, pp. 1432–1440, 2005.

[2] J. H. Jensen and J. A. Helpern, "MRI quantification of non-Gaussian water diffusion by kurtosis analysis," *NMR Biomed.*, vol. 23, no. 7, pp. 698–710, 2010.

[3] E. Wu and M. Cheung, "MR diffusion kurtosis imaging for neural tissue characterization," *NMR Biomed.*, vol. 23, no. 7, pp. 836–848, Aug. 2010.

[4] J. Zhuo and R. P. Gullapalli, "Diffusion kurtosis imaging," in *Neuroimaging Techniques in Clinical Practice*. Cham, Switzerland: Springer, 2020, pp. 215–228.

[5] S. Van Cauter, J. Veraart, J. Sijbers, R. Peeters, U. Himmelreich, F. DeKeyzer, S. Van Gool, F. Van Calenbergh, S. De Vleeschouwer, W. VanHecke, and S. Sunaert, "Gliomas: Diffusion kurtosis MR imaging in grading," *Radiology*, vol. 263, no. 2, pp. 492–501, 2012.

[6] F. F. McKenna, L. Miles, J. S. Babb, D. C. Goff, and M. Lazar, "Diffusion kurtosis imaging of gray matter in schizophrenia," *Cortex*, vol. 121, pp. 201–224, Dec. 2019.

[7] H. Lu, J. H. Jensen, A. Ramani, and J. A. Helpern, "Three-dimensional characterization of non-Gaussian water diffusion in humans using diffusion kurtosis imaging," *NMR Biomed.*, vol. 19, no. 2, pp. 236–247, Apr. 2006.

[8] A. J. Steven, J. Zhuo, and E. R. Melhem, "Diffusion kurtosis imaging: An emerging technique for evaluating the microstructural environment of the brain," *Amer. J. Roentgenol.*, vol. 202, no. 1, pp. W26–W33, Jan. 2014.

[9] E. Fieremans, J. H. Jensen, and J. A. Helpern, "White matter characterization with diffusional kurtosis imaging," *NeuroImage*, vol. 58, no. 1, pp. 177–188, Sep. 2011.

[10] E. E. Sigmund, C. Hu, M. Lazar, M. F. Falangola, J. H. Jensen, and J. A. Helpern, "Diffusion kurtosis imaging (DKI) of *in vivo* human brain at 7T," in *Proc. Int. Soc. Mag. Reson. Med.*, vol. 16, 2008, p. 3331.

[11] R. Heidemann, A. Anwander, T. Feiweier, F. Fasano, J. Pfeuffer, T. Knösche, and R. Turner, "High resolution diffusion-weighted imaging in human at 7T," *NeuroImage*, vol. 47, p. S73, Jul. 2009.

[12] D. Gallichan, "Diffusion MRI of the human brain at ultra-high field (UHF): A review," *NeuroImage*, vol. 168, pp. 172–180, Mar. 2018.

[13] O. F. Gulban, F. De Martino, A. T. Vu, E. Yacoub, K. Uğurbil, and C. Lenglet, "Cortical fibers orientation mapping using *in-vivo* whole brain 7T diffusion MRI," *NeuroImage*, vol. 178, pp. 104–118, Sep. 2018.

[14] O. Speck and K. Zhong, "Diffusion tensor imaging at 7T: Expectations vs. reality check," in *Proc. Int. Soc. Mag. Reson. Med.*, vol. 17, 2009, p. 1462.

[15] D. McClymont, I. Teh, H. J. Whittington, V. Grau, and J. E. Schneider, "Prospective acceleration of diffusion tensor imaging with compressed sensing using adaptive dictionaries," *Mag. Reson. Med.*, vol. 76, no. 1, pp. 248–258, 2016.

[16] B. Hansen, T. E. Lund, R. Sangill, and S. N. Jespersen, "Experimentally and computationally fast method for estimation of a mean kurtosis," *Magn. Reson. Med.*, vol. 69, no. 6, pp. 1754–1760, Jun. 2013.
[17] B. Hansen, N. Shemesh, and S. N. Jespersen, "Fast imaging of mean, axial and radial diffusion kurtosis," *NeuroImage*, vol. 142, pp. 381–393, Nov. 2016.
[18] V. Golkov, A. Dosovitskiy, J. I. Sperl, M. I. Menzel, M. Czisch, P. Sämann, T. Brox, and D. Cremers, "q-space deep learning: Twelve-fold shorter and model-free diffusion MRI scans," *IEEE Trans. Med. Imag.*, vol. 35, no. 5, pp. 1344–1351, May 2016.
[19] B. Hansen and S. N. Jespersen, "Recent developments in fast kurtosis imaging," *Frontiers Phys.*, vol. 5, p. 40, Sep. 2017.
[20] E. K. Gibbons, K. K. Hodgson, A. S. Chaudhari, L. G. Richards, J. J. Majersik, G. Adluru, and E. V. DiBella, "Simultaneous NODDI and GFA parameter map generation from subsampled q-space imaging using deep learning," *Magn. Reson. Med.*, vol. 81, no. 4, pp. 1–13, 2018.
[21] Z. Li, T. Gong, Z. Lin, H. He, Q. Tong, C. Li, Y. Sun, F. Yu, and J. Zhong, "Fast and robust diffusion kurtosis parametric mapping using a three-dimensional convolutional neural network," *IEEE Access*, vol. 7, pp. 71398–71411, 2019.
[22] K. P. Pruessmann, M. Weiger, M. B. Scheidegger, and P. Boesiger, "SENSE: Sensitivity encoding for fast MRI," *Magn. Reson. Med.*, vol. 42, no. 5, pp. 952–962, 1999.
[23] R. Bammer, S. L. Keeling, M. Augustin, K. P. Pruessmann, R. Wolf, R. Stollberger, H.-P. Hartung, and F. Fazekas, "Improved diffusion-weighted single-shot echo-planar imaging (EPI) in stroke using sensitivity encoding (SENSE)," *Magn. Reson. Med.*, vol. 46, no. 3, pp. 548–554, 2001.
[24] R. Bammer, M. Auer, S. L. Keeling, M. Augustin, L. A. Stables, R. W. Prokesch, R. Stollberger, M. E. Moseley, and F. Fazekas, "Diffusion tensor imaging using single-shot SENSE-EPI," *Magn. Reson. Med.*, vol. 48, no. 1, pp. 128–136, Jul. 2002.
[25] R. M. Heidemann, D. A. Porter, A. Anwander, T. Feiweier, K. Heberlein, T. R. Knösche, and R. Turner, "Diffusion imaging in humans at 7T using readout-segmented EPI and GRAPPA," *Magn. Reson. Med.*, vol. 64, no. 1, pp. 9–14, Jul. 2010.
[26] A. C. Zelinski, L. M. Angelone, V. K. Goyal, G. Bonmassar, E. Adalsteinsson, and L. L. Wald, "Specific absorption rate studies of the parallel transmission of inner-volume excitations at 7T," *J. Magn. Reson. Imag.*, vol. 28, no. 4, pp. 1005–1018, Oct. 2008.
[27] M. Lustig, D. L. Donoho, and J. M. Pauly, "Sparse MRI: The application of compressed sensing for rapid MR imaging," *Magn. Reson. Med.*, vol. 58, no. 6, pp. 1182–1195, 2007.
[28] S. J. Holdsworth, S. Skare, R. D. Newbould, and R. Bammer, "Robust GRAPPA-accelerated diffusion-weighted readout-segmented (RS)-EPI: Robust GRAPPA-accelerated DW-RS-EPI," *Magn. Reson. Med.*, vol. 62, no. 6, pp. 1629–1640, Dec. 2009.
[29] J. I. Sperl, T. Sprenger, E. T. Tan, V. Golkov, M. I. Menzel, C. J. Hardy, and L. Marinelli, "Total-variation-regularized compressed sensing reconstruction for multi-shell diffusion kurtosis imaging," in *Proc. Int. Soc. Mag. Reson. Med*, vol. 22, 2014, p. 4465.
[30] I. Chatnuntawech, B. Gagoski, B. Bilgic, S. F. Cauley, K. Setsompop, and E. Adalsteinsson, "Accelerated ^{1}H MRSI using randomly undersampled spiral-based k-space trajectories," *Magn. Reson. Med.*, vol. 74, no. 1, pp. 13–24, Jul. 2015.
[31] H. Pedersen, S. Kozerke, S. Ringgaard, K. Nehrke, and W. Y. Kim, "k-t PCA: Temporally constrained k-t BLAST reconstruction using principal component analysis," *Magn. Reson. Med.*, vol. 62, no. 3, pp. 706–716, 2009.
[32] X. Qu, X. Cao, D. Guo, C. Hu, and Z. Chen, "Combined sparsifying transforms for compressed sensing MRI," *Electron. Lett.*, vol. 46, no. 2, pp. 121–123, Jan. 2010.
[33] S. Ravishankar and Y. Bresler, "MR image reconstruction from highly undersampled k-space data by dictionary learning," *IEEE Trans. Med. Imag.*, vol. 30, no. 5, pp. 1028–1041, May 2011.
[34] C. Huang, C. G. Graff, E. W. Clarkson, A. Bilgin, and M. I. Altbach, "T_2 mapping from highly undersampled data by reconstruction of principal component coefficient maps using compressed sensing," *Magn. Reson. Med.*, vol. 67, no. 5, pp. 1355–1366, May 2012.
[35] Y. Zhu, Q. Zhang, Q. Liu, Y.-X. J. Wang, X. Liu, H. Zheng, D. Liang, and J. Yuan, "PANDA-$T_{1\rho}$: Integrating principal component analysis and dictionary learning for fast $T_{1\rho}$ mapping," *Magn. Reson. Med.*, vol. 73, no. 1, pp. 263–272, 2015.
[36] F. Zong, M. N. d'Eurydice, and P. Galvosas, "Fast reconstruction of highly undersampled MR images using one and two dimensional principal component analysis," *Magn. Reson. Imag.*, vol. 34, no. 2, pp. 227–238, Feb. 2016.
[37] K. H. Jin, D. Lee, and J. C. Ye, "A general framework for compressed sensing and parallel MRI using annihilating filter based low-rank Hankel matrix," *IEEE Trans. Comput. Imag.*, vol. 2, no. 4, pp. 480–495, Dec. 2016.
[38] B. Dietz, E. Yip, J. Yun, B. G. Fallone, and K. Wachowicz, "Real-time dynamic MR image reconstruction using compressed sensing and principal component analysis (CS-PCA): Demonstration in lung tumor tracking," *Med. Phys.*, vol. 44, no. 8, pp. 3978–3989, Aug. 2017.
[39] M. Mardani, E. Gong, J. Y. Cheng, S. S. Vasanawala, G. Zaharchuk, L. Xing, and M. J. Pauly, "Deep generative adversarial neural networks for compressive sensing MRI," *IEEE Trans. Med. Imag.*, vol. 38, no. 1, pp. 167–179, Jan. 2019.
[40] Y. Liu, Q. Liu, M. Zhang, Q. Yang, S. Wang, and D. Liang, "IFR-Net: Iterative feature refinement network for compressed sensing MRI," *IEEE Trans. Comput. Imag.*, vol. 6, pp. 434–446, Nov. 2020.
[41] Y. Zhang, M. Brady, and S. Smith, "Segmentation of brain MR images through a hidden Markov random field model and the expectation-maximization algorithm," *IEEE Trans. Med. Imag.*, vol. 20, no. 1, pp. 45–57, Jan. 2001.
[42] S. M. Smith, M. Jenkinson, M. W. Woolrich, C. F. Beckmann, T. E. J. Behrens, H. Johansen-Berg, P. R. Bannister, M. De Luca, I. Drobnjak, D. E. Flitney, R. K. Niazy, J. Saunders, J. Vickers, Y. Zhang, N. De Stefano, J. M. Brady, and P. M. Matthews, "Advances in functional and structural MR image analysis and implementation as FSL," *NeuroImage*, vol. 23, pp. S208–S219, Jan. 2004.
[43] J. Veraart, D. S. Novikov, D. Christiaens, B. Ades-Aron, J. Sijbers, and E. Fieremans, "Denoising of diffusion MRI using random matrix theory," *NeuroImage*, vol. 142, pp. 394–406, Nov. 2016.
[44] J. L. R. Andersson and S. N. Sotiropoulos, "An integrated approach to correction for off-resonance effects and subject movement in diffusion MR imaging," *NeuroImage*, vol. 125, pp. 1063–1078, Jan. 2016.
[45] A. Tabesh, J. H. Jensen, B. A. Ardekani, and J. A. Helpern, "Estimation of tensors and tensor-derived measures in diffusional kurtosis imaging," *Magn. Reson. Med.*, vol. 65, no. 3, pp. 823–836, Mar. 2011.
[46] L. Qi, Y. Wang, and E. X. Wu, "D-eigenvalues of diffusion kurtosis tensors," *J. Comput. Appl. Math.*, vol. 221, no. 1, pp. 150–157, 2008.
[47] L. Qi, D. Han, and E. X. Wu, "Principal invariants and inherent parameters of diffusion kurtosis tensors," *J. Math. Anal. Appl.*, vol. 349, no. 1, pp. 165–180, Jan. 2009.
[48] I. Daubechies, M. Defrise, and C. De Mol, "An iterative thresholding algorithm for linear inverse problems with a sparsity constraint," *Commun. Pure Appl. Math.*, vol. 57, no. 11, pp. 1413–1457, Nov. 2004.
[49] W. Yin, S. Osher, D. Goldfarb, and J. Darbon, "Bregman iterative algorithms for l_1-minimization with applications to compressed sensing," *SIAM J. Imag. Sci.*, vol. 1, no. 1, pp. 143–168, 2008.
[50] L. Chen, L. Bao, J. Li, S. Cai, C. Cai, and Z. Chen, "An aliasing artifacts reducing approach with random undersampling for spatiotemporally encoded single-shot MRI," *J. Magn. Reson.*, vol. 237, pp. 115–124, Dec. 2013.
[51] K. Person, "On lines and planes of closest fit to system of points in space," *Philos. Mag.*, vol. 2, no. 11, pp. 559–572, 1901.
[52] J. Yang, D. Zhang, A. F. Frangi, and J.-Y. Yang, "Two-dimensional PCA: A new approach to appearance-based face representation and recognition," *IEEE Trans. Pattern Anal. Mach. Intell.*, vol. 26, no. 1, pp. 131–137, Jan. 2004.
[53] M. Turk and A. Pentland, "Eigenfaces for recognition," *J. Cognit. Neurosci.*, vol. 3, no. 1, pp. 71–86, 1991.
[54] J. Taur and C. Tao, "Medical image compression using principal component analysis," *IEEE Trans. Image Process.*, vol. 1, pp. 903–906, Aug. 1996.
[55] H. Hotelling, "Analysis of a complex of statistical variables into principal components," *J. Educ. Psychol.*, vol. 24, no. 6, pp. 417–441, 1933.
[56] J. Velikina, A. Alexander, and A. Samsonov, "A novel approach for T_1 relaxometry using constrained reconstruction in parametric dimension," in *Proc. 18th Int. Soc. Magn. Reson. Med.*, vol. 18, 2010, p. 350.
[57] H. Pedersen, S. Kozerke, S. Ringgaard, K. Nehrke, and W. Y. Kim, "*k-t* PCA: Temporally constrained *k-t* BLAST reconstruction using principal component analysis," *Magn. Reson. Med.*, vol. 62, no. 3, pp. 706–716, 2009.

[58] F. Zong, M. N. d'Eurydice, and P. Galvosas, "Reconstructing undersampled MR images by utilising principal-component-analysis-based pattern recognition," in *Proc. 12th Int. Bologna Conf. Magn. Reson. Pourous Media*, 2014, vol. 22, no. 14, pp. 2014–2021.
[59] A. M. Eskicioglu and P. S. Fisher, "Image quality measures and their performance," *IEEE Trans. Commun.*, vol. 43, no. 12, pp. 2959–2965, Dec. 1995.
[60] Z. Wang, A. C. Bovik, H. R. Sheikh, and E. P. Simoncelli, "Image quality assessment: From error visibility to structural similarity," *IEEE Trans. Image Process.*, vol. 13, no. 4, pp. 600–612, Apr. 2004.
[61] J. L. R. Andersson, S. Skare, and J. Ashburner, "How to correct susceptibility distortions in spin-echo echo-planar images: Application to diffusion tensor imaging," *NeuroImage*, vol. 20, no. 2, pp. 870–888, Oct. 2003.
[62] N. J. Tustison, B. B. Avants, P. A. Cook, Y. Zheng, A. Egan, P. A. Yushkevich, and J. C. Gee, "N4ITK: Improved N3 bias correction," *IEEE Trans. Med. Imag.*, vol. 29, no. 6, pp. 1310–1320, Jun. 2010.
[63] Q. Tong, H. He, T. Gong, C. Li, P. Liang, T. Qian, Y. Sun, Q. Ding, K. Li, and J. Zhong, "Reproducibility of multi-shell diffusion tractography on traveling subjects: A multicenter study prospective," *Magn. Reson. Imag.*, vol. 59, pp. 1–9, Jun. 2019.
[64] B. Hansen and S. N. Jespersen, "Kurtosis fractional anisotropy, its contrast and estimation by proxy," *Sci. Rep.*, vol. 6, no. 1, pp. 1–13, Apr. 2016.

FANGRONG ZONG was born in 1988. She received the bachelor's and master's degrees from China University of Petroleum, Beijing, in 2011 and 2014, respectively, and the Ph.D. degree in physics from Victoria University of Wellington, New Zealand, in 2016.

She is currently an Associate Research Fellow with the Institute of Biophysics (IBP), Chinese Academy of Sciences. She is the Assistant Director of the High Field MR Centre, IBP. Her research involves developing novel diffusion MRI methods and relevant inversion algorithms to obtain tissue microstructure and morphometry. She is working on time-efficient data acquisition and image reconstruction of DKI to clinical applications. Her research interest includes ultra-high field techniques.

JIAXIN DU received the bachelor's degree in physics and the master's degree in particle physics from Central China Normal University and the Ph.D. degree in computational neuroscience from The University of Queensland.

His Ph.D. project focuses on modeling the electric currents generated by neuronal activities and their effects on magnetic resonance (MR) signals. He currently works as a Postdoctoral Research Fellow with the Centre for Advanced Imaging (CAI), where he continues his research in modeling the electric and magnetic signals of neuronal activities in the cortex and designing novel MR protocols to capture the neuronal currents in the cortex. He participates in developing portable ultra-low field MR equipment at CAI.

XIAOFENG DENG was born in 1986. He received the bachelor's and master's degrees in medicine and the M.D. degree from Capital Medical University, Beijing, in 2010, 2013, and 2016, respectively.

He is currently a Neurosurgeon at Beijing Tiantan Hospital, Capital Medical University. His research interests include cerebrovascular diseases and brain plasticity in the circumstance of brain diseases, especially language reorganization.

XUBIN CHAI was born in 1983. He received the B.S. degree from Changzhi Medical College, in 2007, and the M.S. degree from Jinzhou Medical University, in 2011.

He is currently an Assistant Research Fellow with the State Key Laboratory of Brain and Cognitive Science, Institute of Biophysics, Chinese Academy of Sciences. He is working on the research of 7 T MRI techniques in the diagnosis of trigeminal neuralgia and Parkinson's diseases. He has completed more than a thousand neurosurgeries during his career. As the only clinical cooperator of the laboratory, he promotes advanced MRI techniques to be timely applied in clinics.

YAN ZHUO was born in 1963. He received the B.S. degree from Wuhan University, in 1985, and the M.S. degree from China University of Science and Technology, in 1988.

He is currently the Deputy Director of the State Key Laboratory of Brain and Cognitive Sciences. By using functional magnetic resonance imaging (fMRI), he found that the resolving task of topological property produced excitations in the temporal lobe of the left hemisphere and revealing complex brain mechanisms related to topological perception supported by behavioural tests. His research interest includes the development of advanced MRI technologies and applications into cognitive sciences.

A. VIKTOR VEGH received the Ph.D. degree in applied mathematics in the area of electromagnetic wave modeling.

His Ph.D. degree allowed him to pursue a postdoctoral fellowship in MRI hardware design. He has retained an active interest in creating portable low-cost MRI instruments operating at ultra-low magnetic fields. He currently holds a group leader position with the Centre for Advanced Imaging, The University of Queensland, Brisbane, Australia. Since 2010, he has been expanding his research interest to neuroimaging and to his current focus around how mathematical models can be used to create new MRI contrasts reflecting information at scales smaller than the image resolution. Most of his current research time is spent on the research and development of tissue microstructure imaging methods using high and ultra-high field MRI instruments. His work on finding a relationship between tissue microstructure features and mathematical model parameters utilises various MRI contrast mechanisms, such as gradient recalled echo and diffusion-weighted imaging.

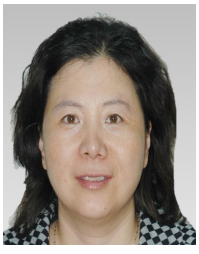

RONG XUE was born in 1965. She received the B.S. degree in electrical engineering from Tsinghua University, Beijing, in 1989, the M.S. degree in biomedical engineering from The Ohio State University, Hsinchu, Columbus, in 1993, and the Ph.D. degree in biomedical engineering from Johns Hopkins University, in 2001.

She is currently the Principal Investigator of neuroimaging with the Institute of Biophysics, Chinese Academy of Sciences. Her research interests include high-field magnetic resonance imaging, parallel imaging, diffusion tensor imaging (DTI), multi-channel transmit/receive coil design and construction, application of MR technologies to human and animal neural anatomical, and functional models with different diseases and functional MRI technical development for cognitive science studies.